

First-principles insights into $NaMgPO_3S$ oxysulfide solid electrolyte

Jian Sun(孙健), Shaohui Ding(丁少辉), Daquan Yang(杨大全), Kan Zhang(张侃), and Huican Mao(毛慧灿)
Citation: Chin. Phys. B, 2026, 35 (**2**): 027105. DOI: 10.1088/1674-1056/adf17d
http://cpb.iphy.ac.cn; http://iopscience.iop.org/cpb

What follows is a list of articles you may be interested in

Two-dimensional kagome semiconductor $Sc_6S_5X_6$ (X = Cl, Br, I) with trilayer kagome lattice

Jin-Ling Yan(闫金铃), Xing-Yu Wang(王星雨), Gen-Ping Wu(吴根平), Hao Wang(王浩), Ya-Jiao Ke(柯亚娇), Jiafu Wang(王嘉赋), Zhi-Hong Liu(刘志宏), and Jun-Hui Yuan(袁俊辉)
Chin. Phys. B, 2026, 35 (**2**): 027102. DOI: 10.1088/1674-1056/ae00b4

First-principles calculations on strain tunable hyperfine Stark shift of shallow donors in Si

Zi-Kai Zhou(周子凯) and Jun Kang(康俊)
Chin. Phys. B, 2025, 34 (**8**): 087102. DOI: 10.1088/1674-1056/addeba

Interacting Dirac semi-metal state in nonsymmorphic Kondo-lattice compound $CeAgSb_2$

Da-Liang Guo(郭达良), and Huan Li(黎欢)
Chin. Phys. B, 2025, 34 (**6**): 067102. DOI: 10.1088/1674-1056/adc6f6

Unveiling the thermal transport mechanisms in novel carbon-based graphene-like materials using machine-learning potential

Yao-Yuan Zhang(章耀元), Meng-Qiu Long(龙孟秋), Sai-Jie Cheng(程赛杰), and Wu-Xing Zhou(周五星)
Chin. Phys. B, 2025, 34 (**6**): 067101. DOI: 10.1088/1674-1056/adca18

Predicted stable two-dimensional semiconductor TiOS materials with promising photocatalytic properties: First-principles calculations

Pan Zhang(张攀), Shihai Fu(付世海), Chunying Pu(濮春英), Xin Tang(唐鑫), and Dawei Zhou(周大伟)
Chin. Phys. B, 2025, 34 (**5**): 057103. DOI: 10.1088/1674-1056/adb687

First-principles insights into $NaMgPO_3S$ oxysulfide solid electrolyte

Jian Sun(孙健)[1,2], Shaohui Ding(丁少辉)[2], Daquan Yang(杨大全)[2,†], Kan Zhang(张侃)[1], and Huican Mao(毛慧灿)[1,‡]

[1] *Department of Materials Science, Key Laboratory of Automobile Materials, MOE and International Center of Future Science, Jilin University, Changchun* 130012, *China*

[2] *State Key Laboratory of Information Photonics and Optical Communications, and School of Information and Communication Engineering, Beijing University of Posts and Telecommunications, Beijing* 100876, *China*

(Received 13 April 2025; revised manuscript received 1 July 2025; accepted manuscript online 18 July 2025)

The development of high-performance solid electrolytes is pivotal for advancing solid-state battery technologies. In this work, we design an oxysulfide-based solid electrolyte $NaMgPO_3S$ by combining bond valence theory and density functional theory calculations. The material features a wide band gap of 4.0 eV and a considerable reduced Na^+ migration barrier of 0.44 eV, a 1.26-eV decrease compared to pristine $NaMgPO_4$ ($\sim$ 1.70 eV). *Ab initio* molecular dynamics simulations further reveal significantly enhanced ionic conductivity in the oxysulfide-based system compared to the pristine oxide structure. In addition, the calculated decomposition energy indicates that the modified material exhibits good moisture stability. Our findings suggest that sulfur-doping strategy can simultaneously achieve improved ionic conductivity and high moisture stability in oxide solid electrolytes, which could pave the way for designing high-performance solid electrolytes.

Keywords: solid electrolytes, first-principles calculations, element doping

PACS: 71.15.Pd, 74.20.Pq, 31.15.A–, 31.15.xw

DOI: 10.1088/1674-1056/adf17d **CSTR:** 32038.14.CPB.adf17d

1. Introduction

Secondary batteries have become indispensable in modern energy storage systems, powering diverse applications from portable electronics to electric vehicles and grid-scale energy storage.[1,2] Currently, most secondary batteries rely on liquid organic electrolytes, which may pose significant safety risks and environmental concerns, such as flammability, solvent leakage, and volatile organic compounds emissions. These limitations have driven substantial interest in solid state electrolytes as an alternative, which can boost safety and achieve higher energy density.[3–6]

For inorganic solid electrolytes, essential performance determinants include ionic conductivity, electrochemical stability window, and interfacial chemical stability. The ion transport performance of solid electrolytes is synergistically regulated by multiple factors such as the openness of the crystal structure, carrier concentration, and site connectivity.[7] Heterovalent doping or ion substitution could enhance carrier concentration through controlled defect introduction.[8] Concurrently, the radius mismatch between dopant and host ions optimizes conduction pathway geometry. Furthermore, selecting framework elements with weaker Li^+ interactions can effectively reduce migration activation barriers. In terms of morphology, constructing a glassy state, a glass-ceramic state, or a composite structure helps to form a disordered and continuous ion channel, and further introducing a nanostructure can significantly enhance the ion transport performance through interface effects.[9]

Ion transport path and ion transport mechanisms analyses are crucial for exploring ionic transport properties. The bond valence method is an efficient method for ion transport path analysis. He *et al*. identified the gaps and connecting segments that constitute the ion transport network by combining the topological path network and the bond valence site energy map, thereby obtaining the geometry and energy distribution of non-equivalent ion transport paths between adjacent lattice sites.[10] Shi *et al*. proposed a software that integrates the Ewald technique and combines the Ewald method with the lattice matching algorithm and bond valence, which is an effective tool for identifying ion transport channels.[11] The ion transport mechanisms in inorganic solid electrolytes include interstitial transport and ion exchange co-transport.[12] Interstitial transport refers to the vacancy transport of conducting ions along adjacent sites in the bulk solid electrolyte or by searching for adjacent vacancies or defect sites in the crystal. Ion exchange co-transport refers to ion transport driven by the interaction between interstitial ions and framework ions and between transport ions. In addition, Shi *et al*. developed a multiscale theoretical method to reveal the Li^+ transport mechanism in SEI membranes and proved that Li^+ can diffuse through the knockout mechanism in Li_2CO_3 SEI membranes.[13] Zhao *et al*. proposed that polyanion rotational motion is an effect worth considering to regulate ion transport.[14]

[†]Corresponding author. E-mail: ydq@bupt.edu.cn

[‡]Corresponding author. E-mail: hcmao@jlu.edu.cn

© 2026 Chinese Physical Society and IOP Publishing Ltd. All rights, including for text and data mining, AI training, and similar technologies, are reserved.

In addition, the electrochemical stability window is an important indicator for measuring the electrochemical performance of solid electrolytes. Therefore, efficient electrochemical window prediction technology is of great significance for screening excellent solid electrolytes. Lin *et al*. proposed a method for predicting the electrochemical stability window with high accuracy. The predicted results are in good agreement with the experimental measurement results, proving the effectiveness of the method.[15] Wang *et al*. also established a database containing information such as electrochemical stability, which facilitates machine learning to accelerate the screening of solid electrolytes.[16]

Sulfide- and oxide-based solid electrolytes are two widely studied categories in solid-state battery research, each presenting distinct advantages and limitations.[17–20] Sulfide electrolytes, exemplified by $Li_{10}GeP_2S_{12}$ (LGPS) and its derivatives, exhibit exceptional ionic conductivity (10^{-2} S/cm),[21–23] comparable to liquid electrolytes. However, their practical application is severely constrained by poor air stability. In contrast, oxide electrolytes demonstrate better electrochemical stability but generally suffer from lower conductivity and interface contact issues. To address these competing limitations, recent advancements have focused on oxysulfide hybrid systems that synergistically combine sulfur and oxygen anions. Li *et al*. combined first-principles calculations and crystal structure prediction techniques to prove that LiAlSO exhibits high ionic conductivity and wide electrochemical window, positioning it as a highly promising solid electrolyte candidate for lithium secondary batteries.[24] Banerjee *et al*. identified $Li_{10}(MS_4)(PO_4)_2$ (L*M*PSO; M = Ge, Sn) as an oxysulfide-based lithium superionic conductor based on ab initio simulation and high-throughput screening.[25] Compared with the sulfur analog L*M*PS, L*M*PSO has good moisture stability and thermodynamic stability. In addition, it has a wider electrochemical stability window and forms a stable interface with high-voltage cathode materials and lithium metal anodes. Kuo *et al*. prepared LiSnOS powders with varying Li/Sn ratios. The LiSnOS with an Li/Sn molar ratio of 2 formed a layered compound $Li[Li_{1/3}Sn_{2/3}(O,S)_2]$, achieving the highest Li–ion conductivity of 1.9×10^{-4} S/cm.[26] The hybrid lithium ion batteries with 30% LiSnOS-filled PVDF-HFP electrolyte showed good charge/discharge performance. The prepared LiSnOS sheet could be stored in air for at least two weeks without phase decomposition, indicating its good air stability and thermodynamic stability. Collectively, these innovations underscore the potential of sulfur-oxygen anion engineering in developing solid electrolytes that simultaneously have improved ionic conductivity and chemical/electrochemical stability for next-generation energy storage systems.

Inspired by the aforementioned research works, our work focuses on an oxide $NaMgPO_4$ as a base material and aims to improve its ionic conductivity by doping sulfur element. Utilizing theoretical simulations, we conducted systematic investigations into the stability, electronic structure and ionic transport characteristics of sulfur-doped $NaMgPO_3S$. The computational results indicate that sulfur–oxygen co-doping stands out as an effective modification strategy for solid electrolyte materials, providing a critical theoretical framework for advancing next-generation solid-state battery technologies.

2. Computational details

All density functional theory (DFT) calculations in this work were conducted using the Vienna *Ab initio* Simulation Package (VASP) code.[27,28] The exchange–correlation interactions were described using the generalized gradient approximation (GGA) with the Perdew–Burke–Ernzerhof (PBE) form.[29,30] A plane-wave cutoff energy of 520 eV was applied, and the Brillouin zone was sampled with a k-point grid spacing of 0.05 Å^{-1}. Structural optimization, including both atomic positions and lattice parameters, was performed with energy and force convergence criteria of 10^{-5} eV and 0.01 eV/Å, respectively. Phonon calculations were carried out using the Phonopy package.[31] The electronic band structures and density of states were calculated using GGA hybrid functional, implemented in the DS-PAW software (2023 A) within the Device Studio program.[28] We used the qua-siempirical bond-valence (BV) method to obtain the possible ionic transportation channels of $NaMgPO_4$ and $NaMgPO_3S$.[32,33] Climbing image nudged elastic band (CI-NEB) calculations, implemented via the VTST code, were performed on supercells with all dimensions exceeding 10 Å to investigate the vacancy-assisted migration mechanism.[34] Each intermediate image was relaxed until atomic forces were below 0.02 eV/Å. Additionally, the *Ab Initio* Molecular Dynamics (AIMD) simulations were performed using supercells, and a Nose–Hoover thermostat was employed to maintain a constant temperature. The simulation temperatures ranged from 900 K to 1300 K with an interval of 100 K, and the simulation duration was 55 ps.[35] The first 5 ps is used to balance the system and the last 50 ps is used to analyze data. The diffusivity is calculated as the slope of the mean squared displacement (MSD) over time interval according to the Einstein relation

$$D = \frac{1}{2Nd\Delta t}\sum_{i=1}^{N}\frac{1}{N_{\Delta t}}\sum_{t=0}^{t_{\mathrm{tot}}-\Delta t}|r_i(t+\Delta t)-r_i(t)|^2, \tag{1}$$

where $d = 3$ is the dimension of the diffusion system, N is the total number of diffusion ions, vector $r_i(t)$ is position of the i-th ion at time t, t_{tot} is the total simulation duration, $N_{\Delta t}$ is the total number of intervals. The ionic conductivity can be calculated according to the Nernst–Einstein relation[36]

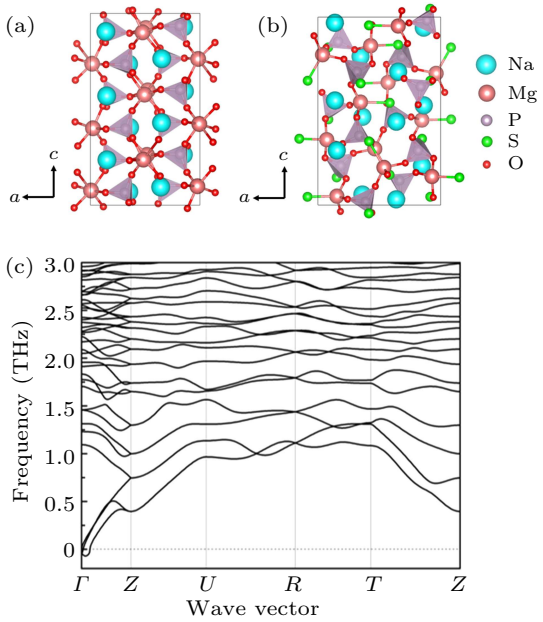
$$\sigma = \frac{Nq^2}{VkT}D, \tag{2}$$

where V is the total volume of the model system, q is the charge of the mobile-ion species, T is the temperature, and k is the Boltzmann constant.

3. Results and discussion

3.1. The crystal structures and stabilities

The pristine $NaMgPO_4$ crystallizes in the $P2_12_12_1$ space group with lattice parameters $a = 8.89$ Å, $b = 6.93$ Å, and $c = 15.50$ Å. As shown in Fig. 1(a), the crystal structure features phosphorus atoms tetrahedrally coordinated by four oxygen atoms, forming a three-dimensional (3D) framework. Partial substitution of oxygen by sulfur generates multiple possible structure configurations. Among all possible configurations, the sulfur arrangement depicted in Fig. 1(b) exhibits the lowest total energy. This energetically favored configuration was therefore selected for subsequent investigations. Full geometric optimization of the sulfur-doped system ($NaMgPO_3S$) reveals a lattice expansion ($a = 10.38$ Å, $b = 8.78$ Å, $c = 15.82$ Å) accompanied by local atomic displacements. Despite these structural adjustments, symmetry analysis via the Materials Studio software confirms that the relaxed structure retains the original $P2_12_12_1$ symmetry, indicating that sulfur substitution does not break the long-range crystallographic order. We have listed the atomic coordinates of Na and Mg in the parent and doped structures and the symmetry operations to find their equivalent atoms (More details seen in the symmetry information section of the supporting information). To verify the dynamic stability of this novel structure, phonon simulations were conducted. As shown in Fig. 1(c), an imaginary frequency mode of approximately -0.07 THz persists at Γ point in the Brillouin zone. This minor imaginary frequency likely arises from inherent limitations of the computational methodology.[37] Consequently, the structure of $NaMgPO_3S$ possesses a certain degree of dynamic stability (More details seen in supporting information). Total energy calculations were performed to assess the thermodynamic stability of the structures. Given the multiple potential decomposition pathways for this compound, we selected two specific decomposition reactions to evaluate the structure stability as shown in Fig. 1(d). The compound exhibits a positive formation energy of 330 meV/atom with respect to decomposition into binary phases for Eq. (1), indicating potential thermodynamic stability. For Eq. (2), the alternative decomposition pathways yield negative formation energies (-52 meV/atom), suggesting thermodynamic preference for ternary phase separation. However, the relatively low reaction energies imply that the compound may exist as a metastable phase or could be stabilized at the synthesis temperature due to the entropy contributions.[24] Specifically, we have reevaluated the formation energy in Eq. (2) by incorporating entropic effects and zero-point vibrational energy. At 500 K, the calculated formation energy of 46.6 meV/atom indicates that $NaMgPO_3S$ exhibits thermodynamic stability, suggesting potential synthesizability above 500 K.



(d)

$$4NaMgPO_3S = Na_2O + Na_2S + MgO + 3MgS + 2P_2O_5 \quad (1)$$

$$12NaMgPO_3S = Na_3PO_4 + 3Na_3PS_4 + 4Mg_3(PO_4)_2 \quad (2)$$

Fig. 1. (a) Crystal structure of $P2_12_12_1$ $NaMgPO_4$. (b) Crystal structure of $P2_12_12_1$ $NaMgPO_3S$. (c) Phono dispersion curves of $NaMgPO_3S$. (d) The decomposition reaction equation of $NaMgPO_3S$. The blue, pink, gray, red, green spheres represent the Na, Mg, P, O, S atoms, respectively.

3.2. Electronic structures

The DFT calculations were carried out to investigate the electronic band structures and density of states (DOS) of pristine $NaMgPO_4$ and sulfur-doped $NaMgPO_3S$. As shown in Fig. 2, the electronic structure analysis reveals distinct characteristics between the two compounds. In $NaMgPO_4$, the valence band maximum (VBM) is dominated by the electronic states of oxygen atoms, while the conduction band minimum (CBM) arises from hybridized oxygen and phosphorus contributions, yielding a wide band gap of 5.0 eV, indicative of excellent electronic insulation. In the sulfur-doped $NaMgPO_3S$ system, partial sulfur substitution significantly modifies the electronic structure. Oxygen atoms retain dominance in the valence band region, whereas sulfur atoms exert distinct regulatory effects near the VBM. At the CBM, the electronic states are primarily dominated by oxygen, sulfur, and phosphorus atoms. This demonstrates a collaborative modulation of electronic states by sulfur and oxygen atoms near the Fermi surface, which governs the material's electronic distribution. Although sulfur doping reduces the band gap to approximately 4.0 eV, the doped structure still maintains strong electronic insulation properties, satisfying the requirements for a solid electrolyte material.

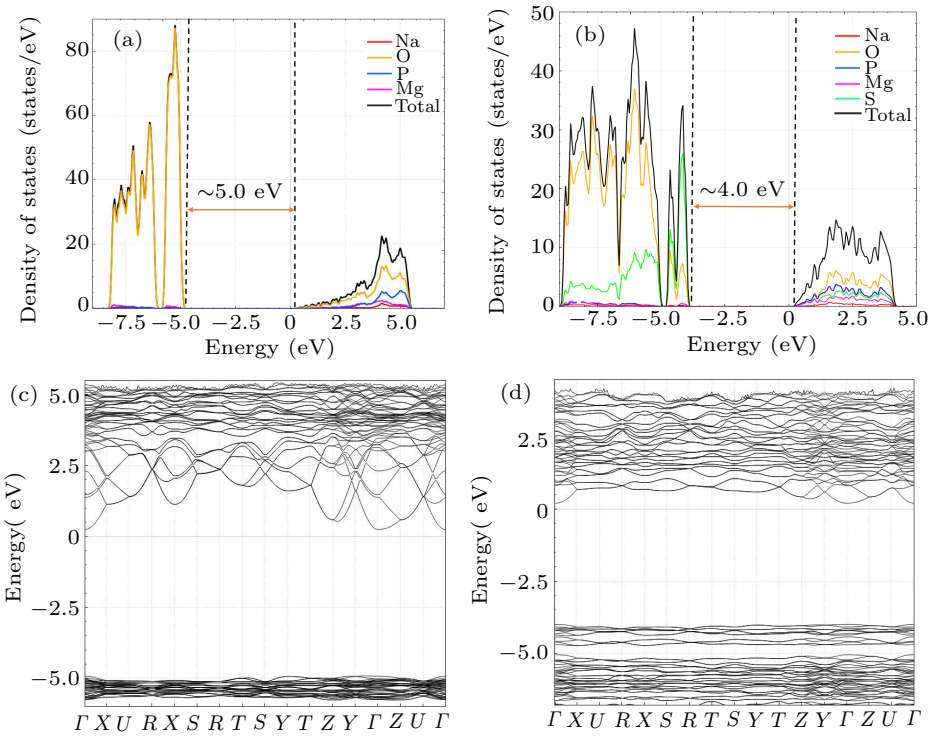


Fig. 2. (a) Projection density of states of crystalline $NaMgPO_4$. (b) Projection density of states of crystalline $NaMgPO_3S$. (c) Band structure of crystalline $NaMgPO_4$. (d) Band structure of crystalline $NaMgPO_3S$.

3.3. Ionic transport mechanism

With the structural stability confirmed, we systematically investigated the Na^+ transport characteristics of $NaMgPO_4$ and its sulfur-doped counterpart $NaMgPO_3S$. The BV method was first employed to map the 3D Na^+ migration pathways. As shown in Fig. 3(a), the preferentially formed Na^+ transport channel of $NaMgPO_3S$ aligns along the *ab*-plane, with the primary diffusion vector parallel to the *a*-axis. This contrasts fundamentally with the parent $NaMgPO_4$, where Na^+ migration predominantly distributes within the *bc*-plane, with the migration direction along the *c*-axis in Fig. 3(c). These results conclusively demonstrate that sulfur doping induces a complete reconfiguration of ionic transport geometry, effectively rotating the principal migration axis from *c* to *a*. For the preferential connectivity paths of the parent structure and doped structure, more details are seen in supporting information.

To quantify the doping-induced kinetic enhancement, we applied the CI-NEB method to calculate the Na^+ migration barriers under vacancy-mediated transport mechanisms. As shown in Fig. 3(b), the sulfur-doped system exhibits a remarkably low activation barrier of 0.44 eV for Na^+ hopping between equivalent low-energy lattice sites, enabling efficient periodic ion migration. In contrast, the pristine structure requires Na^+ ions to overcome a prohibitively high barrier of $\sim$ 1.7 eV to achieve comparable migration (Fig. 3(d)). This dramatic barrier lowering directly correlates with the sulfur-induced lattice expansion and enhanced S–O orbital hybridization, which collectively optimize ionic pathways and lead to a substantial improvement in Na^+ transport.

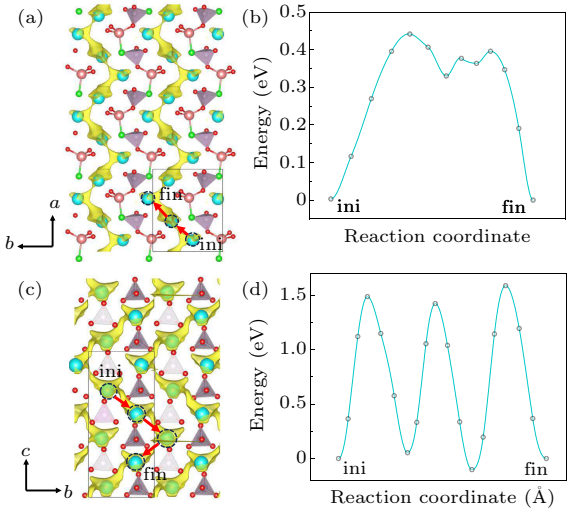


Fig. 3. (a) The periodic continuous migration path of $NaMgPO_3S$ calculated by BV method. (b) The migration barrier of Na^+ in $NaMgPO_3S$ calculated by CI-NEB method. (c) The periodic continuous migration path of $NaMgPO_4$ calculated by BV method. (d) The migration barrier of Na^+ in $NaMgPO_4$ calculated by CI-NEB method. The dotted circle represents the initial or final state of the Na^+ in the CI-NEB calculation process.

3.4. Ionic transport properties

To comprehensively evaluate the ionic transport properties of $NaMgPO_3S$, AIMD simulations were performed. Prior to simulations, the unit cell was expanded along the *b*-axis direction to dimensions exceeding 10 Å per lattice vector, minimizing the finite-size effects. Figure 4(a) presents the temperature-dependent mean squared displacement (MSD) profiles of Na^+. As the temperature increases, the diffusion effect of Na^+ becomes more obvious, and the MSD curve

basically shows a linear relationship. In contrast, the parent $NaMgPO_4$ exhibits negligible MSD growth even at extreme temperature (1400 K) in Fig. 4(c), confirming its intrinsically restricted ionic mobility. The diffusion coefficient at each temperature was extracted from the linear regime of MSD curves using the Einstein relation. As shown in the Arrhenius plot in Fig. 4(b), the calculated room-temperature ionic conductivity reaches 3.0×10^{-6} S/cm, with an activation energy of 0.45 eV derived from the slope, which aligns closely with the migration barrier 0.44 eV derived from the CI-NEB simulations.

In addition, we also evaluated the ion migration behavior of Mg^{2+} by BV method. In the parent and doped structures, Mg^{2+} preferentially migrates along the *b*-axis, as shown in Fig. S5. Figure 4(d) compares the MSD curves of the two compounds at different temperatures. The parent structure maintains minimal Mg^{2+} mobility even at 1300 K, whereas the doped structure exhibits enhanced ion migration with increasing temperature. This demonstrates that sulfur doping improves Mg^{2+} transport properties.

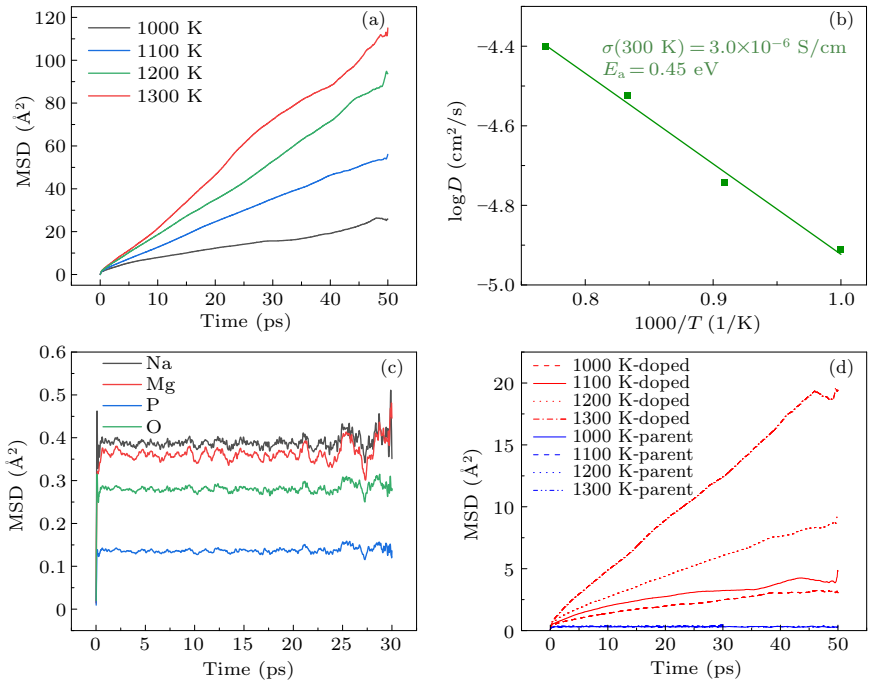
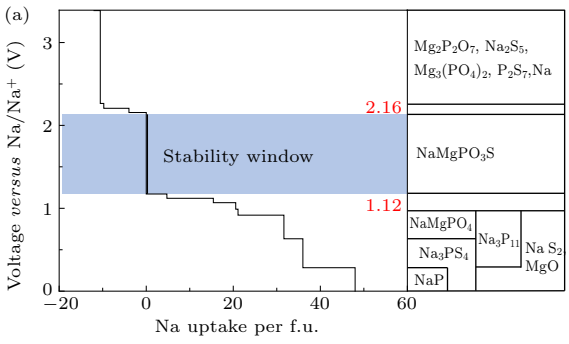


Fig. 4. (a) The MSD–Δ*t* curve from AIMD simulations of $NaMgPO_3S$ supercell over 50 ps at different temperatures. (b) The Arrhenius plot of Na^+ diffusivity *D* as a function of temperature *T* in $NaMgPO_3S$ from AIMD simulations. (c) The MSD–Δ*t* curve from AIMD simulations of $NaMgPO_4$ supercell at 1400 K. (d) The MSD–Δ*t* curve of Mg^{2+} in $NaMgPO_4$ and $NaMgPO_3S$ supercells from AIMD simulations at different temperatures.

3.5. Electrochemical stability and air stability

The electrochemical stability window of solid electrolytes serves as a critical parameter for evaluating their operational voltage range, wherein the material maintains structural integrity without undergoing decomposition or electrochemical reactions. As shown in Fig. 5(a), the calculated electrochemical stability window of $NaMgPO_3S$ spans from 1.12 V to 2.16 V, demonstrating its tolerance within this potential regime. To validate the computational methodology, we benchmarked our results against the well-studied sulfide electrolyte Na_3PS_4. Tian *et al*. reported a theoretical electrochemical stability window of 1.55 V–2.55 V for Na_3PS_4,[38] while noting that such calculations typically yield narrower ranges than experimental cyclic voltammetry measurements due to inherent limitations in accounting for kinetic barriers. Despite this conservative estimation, the electrochemical stability window of $NaMgPO_3S$ aligns closely with that of the mature Na_3PS_4 system, suggesting comparable electrochemical stability and practical viability for solid-state battery applications.



(b) $3NaMgPO_3S+9H_2O = Na_2PO_4+3Mg(OH)_2+3H_2S+2H_3PO_4$ (3)

Fig. 5. (a) The calculated electrochemical window of $NaMgPO_3S$ obtained. (b) The reaction equation of $NaMgPO_3S$ and H_2O.

Furthermore, given the sulfur-containing nature of $NaMgPO_3S$, its moisture stability was evaluated. The reaction energy between $NaMgPO_3S$ and H_2O (Eq. (3)) was calculated to be 91 meV/atom. This thermodynamic analysis implies promising moisture stability, though long-term environmental durability requires experimental verification under humid conditions.

4. Conclusions

In summary, through theoretical calculations, we have discovered an orthorhombic Na–ion conductor $NaMgPO_3S$, which is an oxysulfide-based solid electrolyte formed by sulfur element doping. A wide band gap of 4.0 eV ensures electronic insulation. Phonon dispersion analysis and AIMD simulations confirm robust dynamics stability. CI-NEB and AIMD calculations demonstrate a substantially reduced Na^+ migration barrier coupled with an enhancement in room-temperature ionic conductivity (3.0×10^{-6} S/cm) compared to pristine $NaMgPO_4$. The sulfur–oxygen co-doping strategy provides a certain reference value for the optimization of similar solid electrolytes and the exploration of novel oxysulfide compounds.

Acknowledgements

Project supported by the National Natural Science Foundation of China (Grant Nos. 22473010, 22303114, and 12474372), the Fundamental Research Funds for the Central Universities, Jilin University, the National Key Research and Development Program of China (Grant No. SQ2023YFB2805600), the Natural Science Foundation of Beijing Municipality (Grant No. Z210004), the Fund from the State Key Laboratory of Information Photonics and Optical Communications (Grant No. IPOC2021ZT01), Beijing Nova Program from Beijing Municipal Science and Technology Commission (Grant No. 20230484433), Beijing University of Posts and Telecommunications Excellent Ph.D. Students Foundation (Grant No. CX20241078), and Beijing Natural Science Foundation (Undergraduate Program) (Grant No. QY24218). We gratefully acknowledge HZWTECH for providing computation facilities.

References

[1] Goodenough J B and Park K S 2013 *J. Am. Chem. Soc.* **135** 1167
[2] Dunn B, Kamath H and Tarascon J M 2011 *Science* **334** 928
[3] Goodenough J B and Kim Y 2010 *Chem. Mater* **22** 587
[4] Lin D, Liu Y and Cui Y 2017 *Nat. Nanotechnol.* **12** 194
[5] Bates A M, Preger Y, Torres-Castro L, Harrison K L, Harris S J and Hewson J 2022 *Joule* **6** 742
[6] Yu X, Chen R, Gan L, Li H and Chen L 2023 *Engineering* **21** 9
[7] Gao J, Zhao Y S, Shi S Q and Li H 2015 *Chin. Phys. B* **25** 018211
[8] Lu Z Y, Chen L T, Hu X, Chen S Y, Zhang X and Zhou Z 2024 *Chin. Phys. Lett.* **41** 058201
[9] Ma J Y, Huang Y L, Zhou H J, Wang Y Y, Li J G, Yu X Q, Li H and Li Y 2024 *Chin. Phys. Lett.* **41** 078202
[10] He B, Mi P H, Ye A J, Chi S T, Jiao Y, Zhang L W, Pu B W, Zou Z Y, Zhang W Q and Avdeev M 2021 *Acta Mater.* **203** 116490
[11] Shi W, He B, Pu B W, Ren Y, Avdeev M and Shi S Q 2022 *J. Phys. Chem. A.* **126** 5222
[12] Ren Y, Zou Z Y, Zhao Q, Wang D, Yu J and Shi S Q 2020 *Acta Phys. Sin.* **69** 226601 (in Chinese)
[13] Shi S q, Lu P, Liu Z Y, Qi Y, Hector J L G, Li H and Harris S J 2012 *J. Am. Chem. Soc.* **134** 15476
[14] Zhao Q, Pan L, Li Y J, Chen L Q and Shi S Q 2018 *Rare Met.* **37** 497
[15] Lin S, Lin Y X, He B, Pu B W, Ren Y, Wang G X, Luo Y Q and Shi S Q 2022 *Adv. Energy Mater.* **12** 2201808
[16] Wang X Y, He B, Liu B, Avdeev M and Shi S Q 2024 *Adv. Funct. Mater.* **34** 2406146
[17] Manthiram A, Yu X and Wang S 2017 *Nat. Mater. Rev.* **2** 16103
[18] Kim J J, Yoon K, Park I and Kang K 2017 *Small Methods* **1** 1700219
[19] Chen S, Hu X, Nie L, Yu Y and Liu W 2023 *Sci. China Mater.* **66** 2192
[20] Li S, Wang S, Du G, Liang J, Tong Z, Cui Y, Lin J, Xu X, Liu X, Zhai T and Li H 2025 *Sci. China Mater.* **68** 199
[21] Kamaya N, Homma K, Yamakawa Y, Hirayama M, Kanno R, Yonemura M, Kamiyama T, Kato Y, Hama S, Kawamoto K and Akio M 2011 *Nat. Mater.* **10** 682
[22] Dunn B, Kamath H and Tarascon J M 2011 *Science* **334** 928
[23] Janek J and Zeier W G 2016 *Nat. Energy* **1** 1
[24] Wang X, Xiao R, Li H and Chen L 2017 *Phys. Rev. Lett.* **118** 195901
[25] Banerjee S, Zhang X and Wang L W 2019 *Chem. Mater.* **31** 7265
[26] Kuo D H, Lo R, Hsueh T H, Jan D J and Su C H 2019 *J. Power Sources* **429** 89
[27] Kresse G and Furthmüller J 1996 *Phys. Rev. B* **54** 11169
[28] Blöchl P E 1994 *Phys. Rev. B* **50** 17953
[29] Perdew J P, Ernzerhof M and Burke K 1996 *J. Chem. Phys.* **105** 9982
[30] Perdew J P, Burke K and Ernzerhof M 1996 *Phys. Rev. Lett.* **77** 3865
[31] Togo A and Tanaka I 2015 *Scr. Mater.* **108** 1
[32] Xiao R, Li H and Chen L 2015 *Sci. Rep.* **5** 14227
[33] Adams S and Rao R P 2011 *Phys. Status Solidi A* **208** 1746
[34] Henkelman G, Uberuaga B P and Jónsson H 2000 *J. Chem. Phys.* **113** 9901
[35] Shuichi N 1991 *Prog. Theor. Phys. Suppl.* **103** 1
[36] He X, Zhu Yi, Epstein A and Mo Y 2018 *npj Comput. Mater.* **4** 18
[37] Pallikara I, Kayastha P, Skelton J M and Whalley L D 2022 *Electronic Structure* **4** 033002
[38] Tian Y, Shi T, Richards W D, Li J, Kim J C, Bo S H and Ceder G 2017 *Energy Environ. Sci.* **10** 1150